Reflector Synthesis for Wide-Scanning Focal Plane Arrays

Aleksei Dubok, *Student Member, IEEE*, Ali Al-Rawi, *Student Member, IEEE*, Giampiero Gerini, *Senior Member, IEEE*, and A. Bart Smolders, *Senior Member, IEEE*

***Abstract*— A new complex offset double-reflector configuration for a wideband focal plane array (FPA) is presented which is optimized for Ka-band applications with a scan range of ±20° in the azimuth plane. This configuration is obtained by using a mathematical framework based on geometrical optics which allow us to optimize complex double-reflector FPAs with limited computational effort. The proposed reflector configuration maximizes the number of simultaneously active array elements of the phased-array feed and minimizes the required total number of array elements for this wide scan range. To realize an aperture efficiency of at least 80% at 30 GHz, our concept allows half of the antenna elements in the array to be active during scanning for a scan range of ±10° and at least a quarter of the array elements to be active for a scan range of ±20°. This is a major improvement as compared to the scanning capabilities of focal-plane arrays based on conventional single- and double-parabolic reflector configurations. In addition, the FPA configuration has been optimized for wideband optical true-time-delay beamforming which requires a linear phase distribution along the array elements. We obtained a phase linearity with rms error of 2.81° at 30 GHz. The experiments from the realized prototype demonstrate a good agreement between simulation and measurements and fully prove the required scanning performance over a ±20° scan range. The prototype demonstrates a high directivity up to 46 dBi at 30 GHz and 48 dBi at 40 GHz and reflector efficiency up to 83% at 30 GHz and 77% at 40 GHz.**

***Index Terms*— Antenna array, effective isotropic radiated power (EIRP), focal-plane arrays (FPAs), geometrical optics (GO) modeling, millimeter-waves (mm-waves), reflector antennas, wide scan range.**

I. Introduction

FOCAL-PLANE arrays (FPAs) appear to be a very interesting antenna concept which combines the benefits of phased arrays and traditional reflector-based solutions by offering a high antenna gain, relative low costs and electronic beam scanning over a limited field of view (FoV). Therefore, it has become an interesting alternative to conventional horn-fed reflector antennas in a number of applications, e.g., in radio astronomy [1] and in satellite communication [2], [3]. Moreover, emerging applications such as point-to-point wireless communications, 5G new-radio millimeter-wave (mm-wave) wireless and low-cost Ka-band multifunction radars could be areas in which FPAs can play a major role. These future microwave and mm-wave applications set new requirements on FPA systems such as a wide FoV covering a scan range up to ±20°, large instantaneous bandwidth up to an octave and a high effective isotropic radiated power (EIRP) in transmit mode using silicon-based integrated circuits (ICs) [4]. However, there are still many limitations in the state of the art of FPAs that need to be improved before FPAs can be applied in several of the mentioned applications. First of all, the FoV is limited in conventional FPAs due to the significant beam deviation in the focal plane, and as a result, relatively large arrays are required in the focal plane [5], [6]. This leads to high costs and complexity of the FPA system. Second, the small number of simultaneously active array elements in traditional FPA systems limits the multiple-beam capability [7] and the maximum EIRP [4] that can be achieved. A third limitation in existing FPA concepts is the frequency bandwidth. To obtain a high illumination efficiency, the array spacing needs to be close to $\lambda_0/2$ at the highest frequency of operation [8], where λ_0 is the free-space wavelength. As a result, the mutual coupling between the array elements is rather high and causes the active input impedance of each array element to be different and highly dependent on frequency and angle of incidence [9], [10]. The final limitation is related to the specific beamformer used in this paper. To obtain a wide bandwidth, we will use a novel optical beamforming network that provides multibeam operation over a wide instantaneous bandwidth [11]. The optical beamformer utilizes true-time-delay (TTD) units, implemented in optical ICs. These optical ICs generate frequency-independent time delays with a linear phase [12]. Therefore, a linear phase distribution along the array elements of the FPA is required in order to realize such an optical beamformer circuit [13], [14]. This sets an additional requirement on our FPA system. In this paper, we present the outcome of a study to overcome these limitations. The goal of our work was to develop a wideband FPA system, operating in the frequency band of 20–40 GHz with a scan range up to ±20° in the azimuth plane. The FPA should maximize the EIRP using silicon-based ICs and should minimize the beam deviation in the focal plane region during scanning. Next to this, it should accommodate optical beamforming requiring a linear phase distribution along the array elements.

Manuscript received April 2, 2018; revised December 1, 2018; accepted December 4, 2018. Date of publication January 22, 2019; date of current version April 5, 2019. This work was supported by the Dutch Technology Foundation The Netherlands Organization for Scientific Research under Project FREEBEAM. *(Corresponding author: Aleksei Dubok.)*

The authors are with the Electrical Engineering Department, Eindhoven University of Technology, 5600 MB Eindhoven, The Netherlands (e-mail: a.dubok@tue.nl; a.al.rawi@tue.nl; g.gerini@tue.nl; a.b.smolders@tue.nl).

Color versions of one or more of the figures in this paper are available online at http://ieeexplore.ieee.org.

Digital Object Identifier 10.1109/TAP.2018.2889136

In order to realize these stringent requirements, we propose a new concept for optimal array illumination by the reflector. The idea is based on increasing the number of simultaneously active elements in the FPA to overcome the limitation of a small illuminated region in traditional FPA concepts. By realizing a close to uniform amplitude distribution over the array elements, we can increase the achievable EIRP and system sensitivity. In order to synthesize the optimal configuration of our new complex double-reflector FPA concept, we have developed a mathematical framework based on geometrical optics (GO). We have implemented this framework for single- and double-reflector FPA systems. Various FPA systems with center-fed and offset single- and double-reflector configurations have been optimized and verified with a physical optics (PO) approach using GRASP [15]. The final double-reflector FPA configuration achieves the required scanning range with a compact phased-array feed (PAF), which has at least half of the array elements simultaneously active during scanning. In our study, we have used the classical prime-focus reflector with a diameter $D = 0.8$ m and $F/D = 0.6$ (with F the reflector focal length) as a reference configuration to evaluate the performance improvement of the optimized reflector configurations. In summary, this paper presents the following new scientific contributions.

1) A parametric mathematical framework using GO has been implemented for single- and double-reflector optimization for FPA systems.
2) A new type of reflector concept is proposed with a very compact PAF to realize wide-angle scanning over a wide bandwidth.
3) The proposed reflector configuration maximizes the ratio of active array elements in FPAs and provides a close to linear phase distribution along the PAF.

The structure of this paper is as follows. Section II describes the illumination challenges of classical prime-focus reflectors and describes the ideal array illumination. Section III discusses the mathematical GO framework that is used to synthesize the optimal single- and double-reflector FPA systems. In Section IV, we present the simulation results of the different optimized reflector configurations. Finally, in Section V, we provide the experimental results from the 20 to 40 GHz prototype FPA system with improved scanning capabilities.

II. Limitations of Classical Parabolic Prime-Focus Reflectors and Ideal Array Illumination

The electric-field distribution in the focal plane of a classical prime-focus reflector behaves according to the well-known distribution of so-called Airy rings, corresponding to zeros of the Bessel function of first kind and order 1 along the aperture radius r [16]. The electric field in the focal plane of a classical prime-focus reflector with $F/D = 0.6$ and $D = 0.8$ m is presented in Figs. 1–3 for broadside, 10°, and 20° scanning, respectively, in the frequency band from 20 to 40 GHz. The focal plane position is defined based on the location of the focal point as illustrated in Fig. 1. We can observe that in case of scanning, the region of maximum power is

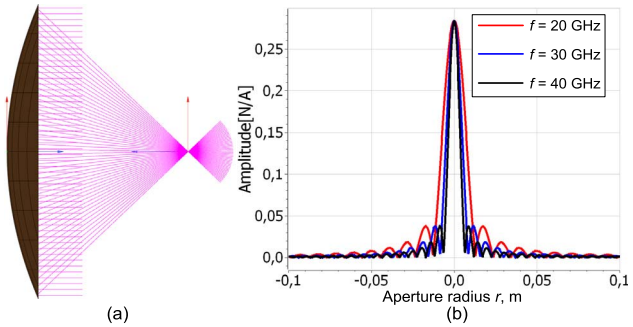

Fig. 1. (a) Reflector configuration. (b) Electric-field cuts in the focal plane for broadside operation of a prime-focus reflector with $F/D = 0.6$ and $D = 0.8$ m.

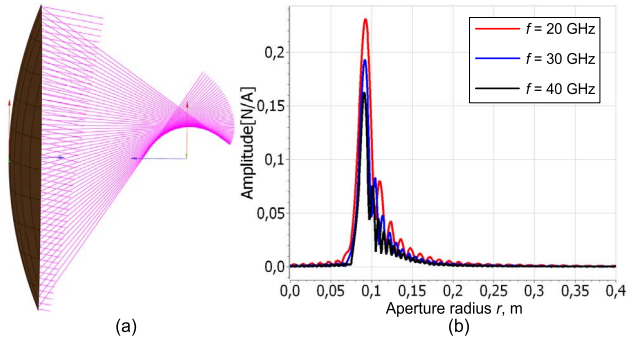

Fig. 2. (a) Reflector configuration. (b) Electric-field cuts in the focal plane for 10° scan angle of a prime-focus reflector with $F/D = 0.6$ and $D = 0.8$ m.

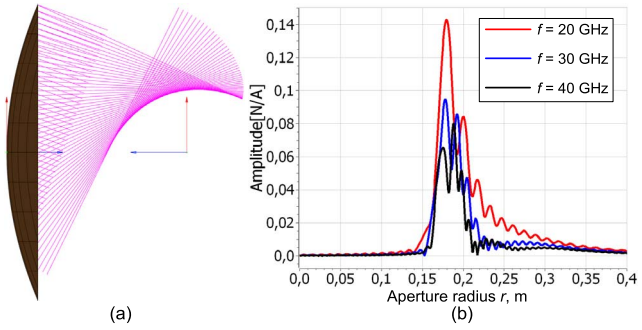

Fig. 3. (a) Reflector configuration. (b) Electric-field cuts in the focal plane for 20° scan angle of a prime-focus reflector with $F/D = 0.6$ and $D = 0.8$ m.

broadened but significantly shifted away from the array center. The corresponding aperture efficiency distribution for the electric-field cuts of Figs. 1–3 is presented in Fig. 4. The aperture efficiency estimation includes the radiation efficiency of the reflector, taper efficiency, spill-over efficiency, and polarization efficiency. It is determined according to [17].

According to Fig. 4, the illuminated region in the focal plane for normal incidence is relatively small. With using an array grid with $\lambda_0/2$ spacing at the center frequency, only a few elements will be active. In case of 10° and 20° scanning, the required array size is significantly increased as illustrated in Fig. 4. In addition, most of the array elements will not be active at the same time. Therefore, the ratio of active elements to the total number of array elements is low and,

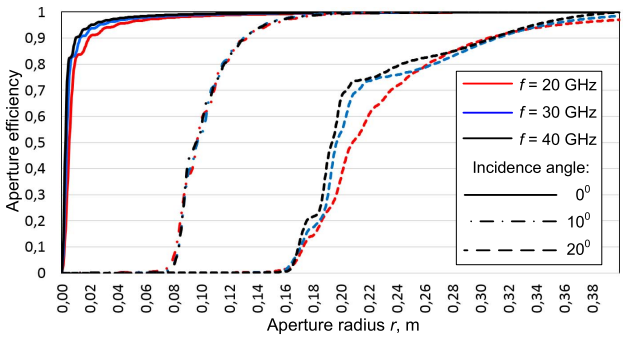

Fig. 4. Aperture efficiency in the focal plane for different angles of incidence of a classical prime-focus reflector with $F/D = 0.6$ and $D = 0.8$ m.

as a result, the FPA is used inefficiently. This will limit the achievable EIRP level and beam scanning capabilities. Moreover, to provide scanning up to ±20° in the azimuth plane, the dimension of the array should be at least 0.52 m to achieve an 80% aperture efficiency with a reflector size of 0.8 m. In other words, the PAF dimension is about 65% of the reflector diameter, which is undesirable. Therefore, we need to minimize the beam deviation during scanning in order to limit the FPA size and overall system cost. Another possible problem is related to the required linear phase distribution. In [17], it was shown that even at broadside this cannot be realized with a classical prime-focus FPA.

III. Mathematical Principles of Reflector Synthesis Based on Geometrical Optics

To design an FPA system with improved PAF illumination characteristics, we first need to define an "ideal" focal-plane illumination. Compared to the traditional prime-focus reflector, the ideal reflector should provide a close to uniform amplitude illumination and linear or constant phase along the PAF. In order to have a sufficient number of simultaneously active PAF elements, the illuminated array size should be at least a few centimeters at 30 GHz. For example, using an ideal array size of 4 cm^2, 16 elements will be available with element spacing of $\lambda_0/2$ at 30 GHz.

To develop a model of the FPA system which could approach an "ideal" focal-plane illumination, it is necessary to optimize the shape of the main- and sub-reflectors. The optimized model is then verified using a PO with more accurate and computationally more intensive model. Our model uses an GO approach, which applies Snell's law according to [18]–[20]. When we describe the reflector surface as a mathematical function and divide the surface into a finite number of points, it is possible to find the normal at each point of the reflector. On the basis of Snell's law, the reflected wave in each reflector point can be calculated. In this way, the field distribution in the array plane can be determined and compared to the ideal illumination, resulting in a cost function used in our optimization process. Based on this approach, we have developed and implemented a GO optimization code for different types of reflectors: 2-D center-fed reflector model with a single and double reflector, 3-D offset reflector model with a single and double reflector. A brief explanation of the

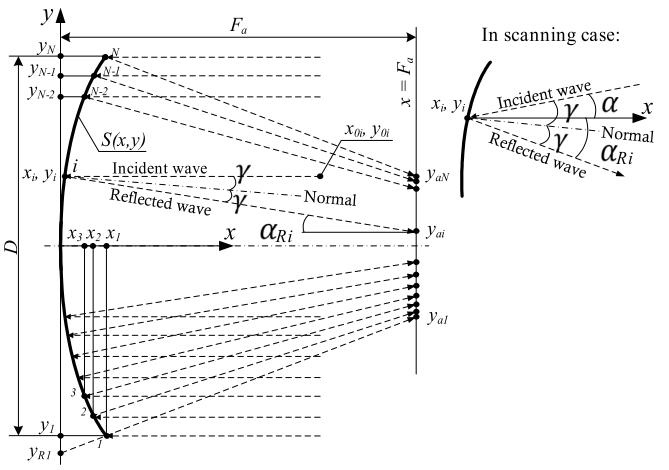

Fig. 5. 2-D model of the symmetric center-fed single reflector.

mathematical principles is presented below for the case of a symmetrical center-fed single reflector and for a complex offset double-reflector FPA which provides wide scanning properties.

A. 2-D Center-Fed Single-Reflector Model

The symmetrical center-fed reflector can be expressed in a 2-D coordinate system, as shown in Fig. 5. To find an optimal shape for wide-angle scanning, we have defined our reflector in terms of a second-order polynomial

$$S(x, y) = A_{xx}x^2 + 2A_x x + A_{yy}y^2 = 0 \tag{1}$$

where A_{ij} are polynomial coefficients which will be determined by our optimization process. The reflector center is located in the center of the coordinate system. Discretization of the reflector to the N points along the y-coordinate gives

$$y_i = y_1 \ldots y_N, \quad y_1 = -\frac{D}{2}, \quad y_N = \frac{D}{2} \tag{2}$$

where D is the diameter of the reflector. To find the corresponding x coordinate, it is necessary to solve (1) as a quadratic equation

$$x_i = -\frac{A_x \pm \sqrt{A_x^2 - A_{xx}A_{yy}y_i^2}}{A_{xx}}. \tag{3}$$

From the two possible solutions of x_i in (3), the solution with a real value should be selected in order to have a realistic shape of the reflector. In case, $S(x, y)$ is a closed surface, like part of an ellipsoid or sphere, the nearest value of x_i to the center of the coordinate system should be chosen. As a result, N reflector points are defined by the coordinates (x_i, y_i) (see Fig. 5).

The linear equation of the normal at point (x_i, y_i) can be set via partial derivatives of $S(x, y)$ in the following way

$$\frac{x - x_i}{\frac{\partial S(x_i, y_i)}{\partial x}} = \frac{y - y_i}{\frac{\partial S(x_i, y_i)}{\partial y}} \tag{4}$$

where $(\partial S(x_i, y_i)/(\partial x = 2A_{xx}x_i + 2A_x))$ and $(\partial S(x_i, y_i)/\partial y) = 2A_{yy}y_i$. In the form of a linear equation in

xy-coordinates, the normal could be expressed as

$$y = (x - x_i)\frac{2A_{yy}y_i}{2A_{xx}x_i + 2A_x} + y_i. \tag{5}$$

Snell's law states that the angle γ between the incidence wave and the normal to the surface is equal to the angle between the normal and the reflected wave. The $\tan(\gamma)$ between two straight lines given by equations $y = k_1x + b_1$ and $y = k_2x + b_2$, is calculated by

$$\tan(\gamma) = \frac{k_2 - k_1}{1 + k_1k_2}. \tag{6}$$

For an incidence wave, we find that: $k_1 = \tan(\alpha)$ and $k_2 = (2A_{yy}y_i/(2A_{xx}x_i + 2A_x))$; for a reflected wave we obtain: $k_1 = (2A_{yy}y_i/(2A_{xx}x_i + 2A_x))$ and $k_2 = \tan(\alpha_{Ri})$. Applying Snell's law gives

$$\tan(\gamma) = \frac{\tan(\alpha) - \frac{2A_{yy}y_i}{2A_{xx}x_i+2A_x}}{1 + \tan(\alpha)\frac{2A_{yy}y_i}{2A_{xx}x_i+2A_x}} = \frac{\frac{2A_{yy}y_i}{2A_{xx}x_i+2A_x} - \tan(\alpha_{Ri})}{1 + \frac{2A_{yy}y_i}{2A_{xx}x_i+2A_x}\tan(\alpha_{Ri})}. \tag{7}$$

Equation (7) could be solved for $\tan(\alpha_{Ri})$ as

$$\tan(\alpha_{Ri}) = \frac{\tan(\alpha)\left(\frac{2A_{yy}y_i}{2A_{xx}x_i+2A_x}\right)^2 + 2\frac{2A_{yy}y_i}{2A_{xx}x_i+2A_x} - \tan(\alpha)}{2\tan(\alpha)\frac{2A_{yy}y_i}{2A_{xx}x_i+2A_x} + 1 - \left(\frac{2A_{yy}y_i}{2A_{xx}x_i+2A_x}\right)^2}. \tag{8}$$

The array plane is a set of points located in the plane $x = F_a$. The y-coordinates of the reflected waves at the array plane y_{ai} gives a distribution of the field as a set of coordinates, which can be written as

$$y_{ai} = F_a\tan(\alpha_{Ri}) + y_{Ri}. \tag{9}$$

To define the optimum amplitude distribution as a set of coordinates of the N reflected rays in the array plane, we have to define the ideal distribution of the coordinates of the N-points, indicated by y_{ai}. This distribution corresponds to the "ideal" focal-plane illumination with uniform amplitude along the PAF. When we consider a symmetric 2-D reflector, the ideal focal area would have a uniform radial distribution. Therefore, the wanted distribution due to the rays reflected at the N points, would take the following form:

$$\begin{aligned}
\mathrm{Am}_{ai}^{w} &= \mathrm{Am}_{ai}^{0}\left(1 + \frac{L_y}{2} - \sqrt{\left(\frac{L_y}{2}\right)^2 + \left(\mathrm{Am}_{ai}^{0} + \frac{L_y}{2}\right)^2}\right), \\
&\quad \mathrm{Am}_{ai}^{0} < 0 \\
\mathrm{Am}_{ai}^{w} &= \mathrm{Am}_{ai}^{0}\left(1 + \frac{L_y}{2} - \sqrt{\left(\frac{L_y}{2}\right)^2 - \left(\mathrm{Am}_{ai}^{0} + \frac{L_y}{2}\right)^2}\right), \\
&\quad \mathrm{Am}_{ai}^{0} > 0
\end{aligned} \tag{10}$$

where $\mathrm{Am}_{ai}^{0} = -(L_y/2) + (L_y/(N-1))(i-1)$, for $i = 1 \ldots N$ and where L_y is the size of the array along the y-direction. It is important to note that the array size should be at least a few wavelengths. Otherwise, we will have a significant difference between the GO and PO simulation results due to the ray caustics in the array plane [21]. Based on the obtained coordinates y_{ai} and the wanted distribution, defined in (10), the amplitude cost function can be defined as a standard deviation

$$\mathrm{Cost}_{Amp} = \sqrt{\frac{1}{N}\sum_{i=1}^{N}\left(\mathrm{Am}_{ai}^{w} - y_{ai}\right)^2}. \tag{11}$$

The wave front has been defined in front of the reflector as a set of points with coordinates (x_{0i}, y_{0i}) (see Fig. 5). The total length of each path for each ray can be calculated as

$$L_i = \sqrt{(x_i - x_{0i})^2 + (y_i - y_{0i})^2} + \sqrt{(F_a - x_i)^2 + (y_{ai} - y_i)^2}. \tag{12}$$

To estimate the phase linearity along the array, the standard deviation for the phase path can be defined by

$$\mathrm{Cost}_{Ph} = \sqrt{\frac{1}{N}\sum_{i=1}^{N}\left((L_i - L_{N/2})/\lambda_0\right)^2}. \tag{13}$$

Normalization to the wavelength, λ_0 makes the function invariant to the chosen frequency. One of the main optimization goals is to minimize the deviation of the field in the array plane during scanning. The deviation of the reflected waves in the array plane Δ_{y_a} can be determined by calculation of the standard deviation of the field distributions in case of normal incidence versus the scan case

$$\mathrm{Cost}_{\Delta} = \Delta_{y_a} = \sqrt{\frac{1}{N}\sum_{i=1}^{N}\left(y_{ai}^{n} - y_{ai}\right)^2} \tag{14}$$

where y_{ai}^{n} are the y-coordinates of the reflected waves at the array plane in case of normal incidence. In case of scanning, the amplitude cost function should be corrected, in order to include the fact that the overall array distribution is shifted along the x-axis

$$\mathrm{Am}_{ai}^{w} = \mathrm{Am}_{ai}^{wn} + \Delta_{y_a} \tag{15}$$

where A_{ai}^{wn} is the distribution in case of normal incidence. The total cost function is a combination of amplitude, phase, and deviation cost functions with adjusted coefficients

$$Cost = K_{sh}\mathrm{Cost}_{\Delta} + K_{Amp}\mathrm{Cost}_{Amp} + K_{Ph}\mathrm{Cost}_{Ph} \tag{16}$$

where K_{sh}, K_{Amp}, and K_{Ph} are weighting coefficients, which will be determined empirically. The obtained cost function can be used to estimate how a specific shape of the reflector is suitable for the illumination of the array for broadside or in case of scanning. By varying the A_{ij} polynomial coefficients, the optimization algorithm provides the most optimal configuration of the reflector according to the GO approach. The proposed optimization algorithm is extremely fast and allows to check thousands of reflectors shapes per second. This is one of the main reasons of using a GO model instead of a PO approach, which is more accurate. Furthermore, one of the main advantages of the presented approach is the possibility to increase the complexity of the reflector by introducing a discontinuity in the reflector, like the well-known ring-focused reflector is one of the particular examples of such a configuration [22].

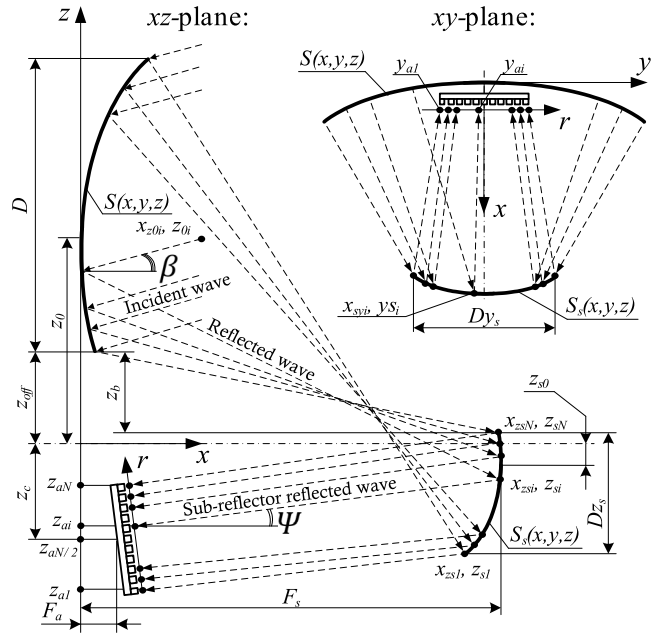

Fig. 6. 3-D offset double-reflector model.

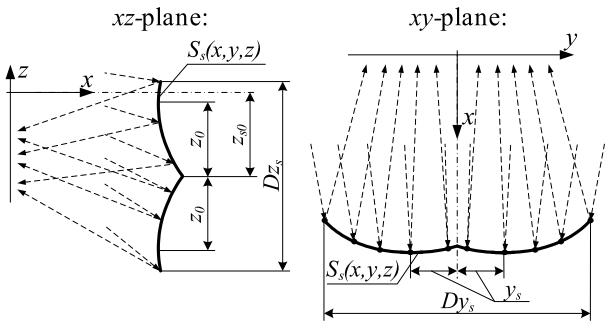

Fig. 7. "Complex" subreflector model with discontinuities of the 3-D offset reflector.

B. 3-D Complex Offset Double-Reflector Model

In case of a double reflector configuration, the obtained designs represent imaging reflector systems, which also could be solved as a lens antenna as demonstrated in [23]. However, the presented approach in [23] is limited to reflectors with a high magnification factor $M = D/D_s \gg 1$, where D_s is the size of the subreflector. At the same time, for double-reflector systems, relatively large subreflectors are required in case of wide-angle scanning [17]. By using an offset configuration as shown in Fig. 6, blockage can be avoided. The reflector surface can now be expressed in terms of a second-order polynomial

$$S(x,y,z) = A_{xx}x^2 + 2A_x x + A_{yy}y^2 + A_{zz}(z-z_0)^2 + 2A_{yz}y(z-z_0) = 0 \quad (17)$$

where A_{ij} are polynomial coefficients and z_0 is the shift of the polynomial function along the z-axis. Note that the vertical offset z_b between the array and reflector should be at least a few wavelengths in order to avoid blockage and diffraction from the edges of the reflector and array. Mutual reflections between the reflector and array are also avoided in this case. In addition, a proper choice of the array position z_c avoids multiple reflections between the main reflector, subreflector and array. The reflector discretization along the y-axis and the determination of the reflected waves from the main reflector is done in a similar way as for the center-fed reflector. Along the z-axis we now have

$$z_i = z_1 \ldots z_N, \quad z_1 = z_{\text{off}}, \quad z_N = z_1 + D. \quad (18)$$

Solving for the intersection of the reflected wave from the main reflector and the subreflector provides the interaction points on the subreflector surface: x_{ysi} and y_{si} (in the xy plane), x_{zsi} and z_{si} (in the xz plane). The reflected wave from the surface of the subreflector is defined in a similar way as the reflection from the main reflector. The position of the array is close to the main reflector, as illustrated in Fig. 6.

To obtain wide-scanning properties, we have applied additional design features to the subeflector geometry, as illustrated in Fig. 7. The shaped subreflector with two different discontinuities in the xy and xz planes is defined by

$$\begin{aligned}
S_s(x,y,z) &= B_{xx}(x-F_s)^2 + 2B_x(x-F_s) + B_{yy}(y-y_s)^2 \\
&\quad + B(z-x_s-z_{s0})^2 + 2B_{yz}(y-y_s)(z-z_s-z_{s0}) \\
&= 0 \text{ when } y>0, z>0 \\
S_s(x,y,z) &= B_{xx}(x-F_s)^2 + 2B_x(x-F_s) + B_{yy}(y+y_s)^2 \\
&\quad + B_{zz}(z-z_s-z_{s0})^2 + 2B_{yz}(y+y_s)(z-x_s-z_{s0}) \\
&= 0 \text{ when } y<0, z>0 \\
S_s(x,y,z) &= B_{xx}(x-F_s)^2 + 2B_x(x-F_s) + B_{yy}(y-y_s)^2 \\
&\quad + B_{zz}(z+z_s-z_{s0})^2 + 2B_{yz}(y-y_s)(z+x_s-z_{s0}) \\
&= 0 \text{ when } y>0, z<0 \\
S_s(x,y,z) &= B_{xx}(x-F_s)^2 + 2B_x(x-F_s) + B_{yy}(y+y_s)^2 \\
&\quad + B_{zz}(z+z_s-z_{s0})^2 + 2B_{yz}(y+y_s)(z+x_s-z_{s0}) \\
&= 0 \text{ when } y<0, z<0
\end{aligned} \quad (19)$$

where F_s is the subreflector position along the x-axis and B_{ij} are subreflector polynomial coefficients, z_{s0} is the shift of the polynomial function along the z-axis, β the angle of rotation of the whole system in the xz plane, Ψ the feeding angle of the array, z_s is a shift in the polynomial function of the subreflector along the z-coordinate and y_s a shift along the y-coordinate. We have applied the same cost function as defined in (16) to optimize the offset double-reflector system.

In summary, in this section, we have derived a direct relation between the shape of the reflectors and the total cost function. The shape of the reflectors can be expressed in terms of polynomial coefficients as in (1), (17), and (19) including design features like reflector shape discontinuities and the shifts of the polynomial function along the coordinates axis. The total cost function is presented as a combination of different optimization goals in (16). By varying the ratio between the cost functions of the amplitude distribution (11), the phase linearity along the array (13) and the deviation of the field in the array plane during scanning (14), it is possible to optimize the reflectors for a particular application.

We have demonstrated our approach for a symmetrical center-fed single reflector and for a complex offset double-reflector FPA. Nevertheless, our concept and formulation

is universal and can be applied to all kinds of reflectors. In Section IV, we will apply our optimization approach to a number of reflector systems with increasing complexity.

IV. Optimization of Single and Double-Reflector Configurations

We have optimized single- and double-reflector configurations with the mathematical model of Section III for two specific situations: 1) no scanning (broadside) and 2) beam scanning up to $+/-20°$. For broadside operation, the goal is to obtain a uniform amplitude and linear phase distribution. In case of scanning, an additional goal is the minimization of the illumination deviation. The following reflector configurations have been optimized and investigated for broadside operation:

1) single reflector with discontinuity;
2) complex double reflector;
3) complex offset double reflector.

The following reflector configurations have been investigated for wide-angle scanning:

1) complex double center-fed reflector;
2) complex offset double reflector.

The "complex" configurations use a discontinuity in the subreflector shaping. Note that the traditional single-reflector configurations have already been investigated for wide-angle scanning in [24]. All investigated configurations include the axial displacement of the array. We have used a PAF with a length of 4 cm, which corresponds to $4\lambda_0$ at 30 GHz. The size of the main reflector is 80 cm for all designs. All optimizations have been done with our mathematical GO model implemented in MATLAB and is dedicated exclusively to the reflector shape optimization. We have used a Monte-Carlo type of algorithm to minimize the cost function in the optimization. The resulting optimized reflector configurations have been simulated in GRASP [15] by means of GO and PO. The PO simulations include the physical theory of diffraction [15]. A comparison of the performance of all optimized configurations is provided in Section IV-F.

A. Single Reflector With Discontinuity

A single parabolic reflector with discontinuity is shown in Fig. 8. The obtained optimal polynomial coefficients and other relevant variables are provided in Table I.

The reflector configuration and corresponding field distribution in the array plane are shown in Fig. 9. From Fig. 9(c), it is clear that the field distribution is more uniform over the array as compared to the classical prime-focus reflector. The phase distribution in the array plane of Fig. 9(d) is significantly improved compared to a classical prime-focus reflector. The linearity of the phase distribution at 30 GHz shows an rms error of 2.02°.

B. Complex Double Reflector

Double-reflector concepts (Fig. 10) provide more degrees of freedom for optimization as compared to single-reflector configurations. For the broadside-scan case, the obtained optimal polynomial coefficients and other relevant dimensions are provided in Table II.

The discontinuity variables Δ_y and y_0 are equal to zero. Therefore, both optimized reflectors have a continuous shape and are easy to produce. The size of subreflector D_s is significantly smaller than that of the main reflector, limiting the reduction of the aperture efficiency due to blockage to

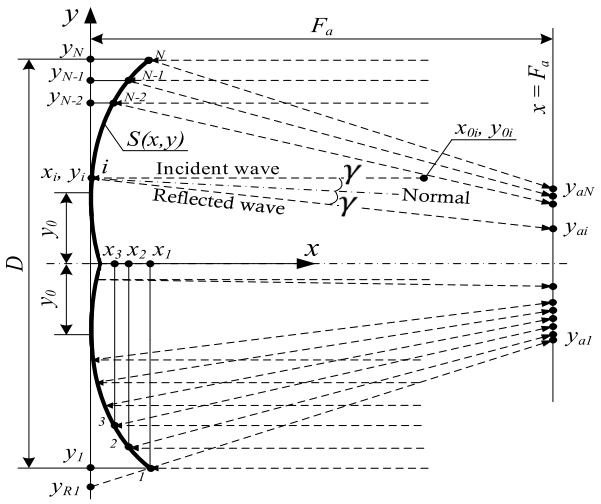

Fig. 8. 2-D center-fed reflector model. Single-complex reflector with a discontinuity in the center.

TABLE I
Optimal Polynomial Coefficients and Dimensions of a Single Reflector With Discontinuity

Variable	Obtained value	Variable	Obtained value
A_{xx}	0.151	A_{yz}	0
A_{yy}	2.0985	F_a	0.48 m
A_x	-2.115	y_0	0.0312 m
A_{zz}	2.0985	D	0.8 m

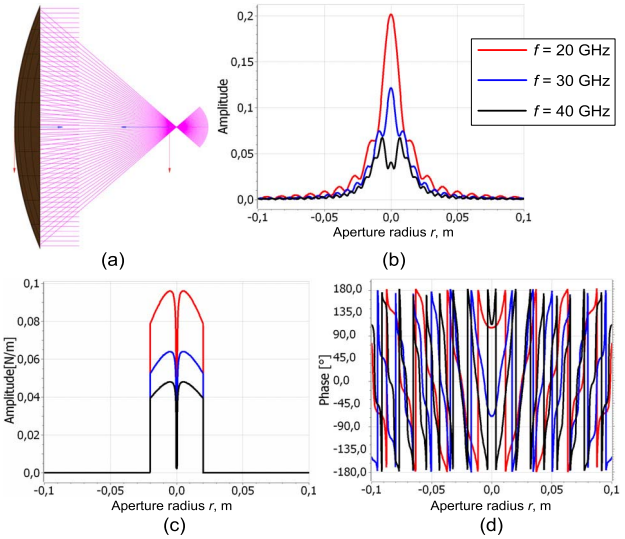

Fig. 9. (a) Single-reflector configuration with discontinuity in the center, broadside situation. (b) Electric-field cuts in the array plane based on PO simulation. (c) Electric-field cuts in the array plane based on GO simulation. (d) Phase distribution based on PO simulation in the array plane.

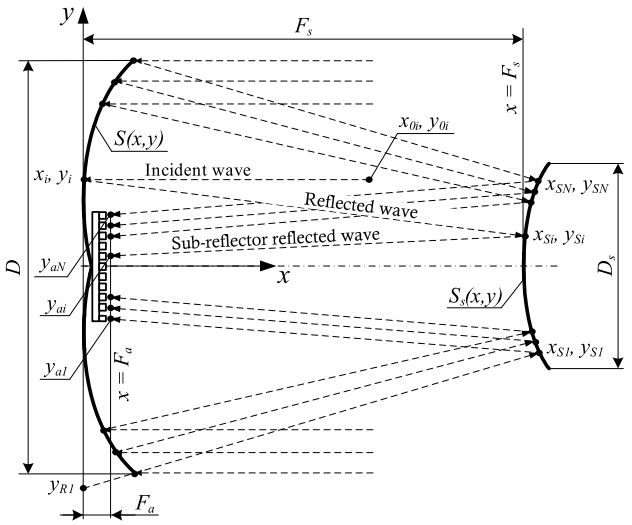

Fig. 10. 2-D center-fed double-reflector model.

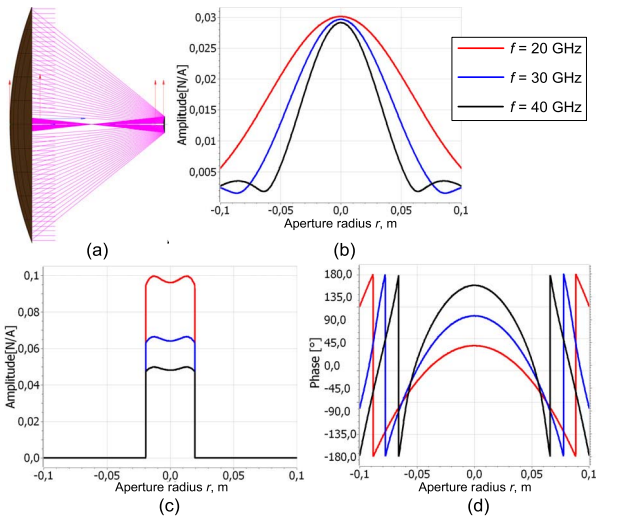

Fig. 11. (a) Double-reflector configuration, broadside situation. (b) Electric-field cuts in the array plane based on PO simulation. (c) Electric-field cuts in the array plane based on GO simulation. (d) Phase distribution based on PO simulation in the array plane.

TABLE II

OPTIMAL POLYNOMIAL COEFFICIENTS AND DIMENSIONS OF A COMPLEX DOUBLE REFLECTOR. OPTIMIZED FOR BROADSIDE SCAN ONLY

Variable	Obtained value	Variable	Obtained value
A_{xx}	0.0735	B_{xx}	2.952
A_{yy}	1.215	B_{yy}	4.977
A_x	-1.325	B_x	-0.456
A_{zz}	1.215	B_{zz}	4.977
A_{yz}	0	B_{yz}	0
F_s	0.507 m	F_a	0.1 m
Δ_y	0 m	y_0	0 m
D_s	0.054 m	D	0.8 m

about 0.5%. The field distribution in the array plane using GO and PO is provided in Fig. 11.

C. Complex Double Center-Fed Reflector

Double-reflector concepts (Fig. 12) include a discontinuity in the subreflector surface. According to [24], wide-angle scanning up to ±20° requires a very large subreflector. For center-fed models, this leads to a significant blockage and energy loss. In addition, double-reflector configurations have another limitation in case of scanning caused by the amplification of the angle of incidence on the array surface [25], [26]. As a result, even a small beam deviation of the incident wave causes a significant shift of the illuminated array region. As a consequence, the array size should be very large. Nevertheless, it is interesting to investigate a fictitious model of the complex double reflector in case of wide-angle scanning, where the effects of blockage are ignored. This model allows to estimate the potential to use double-reflector configurations for wide-angle scanning and can be used as a reference model for offset configurations. The obtained optimal polynomial coefficients and other relevant dimensions are shown in Table III.

Similar to the broadside case, the discontinuity variables Δ_y and y_0 are zero. As a result, both reflectors have a continuous shape. The size of subreflector D_s is not limited for this configuration and, as a result, the blockage is 100%. It makes

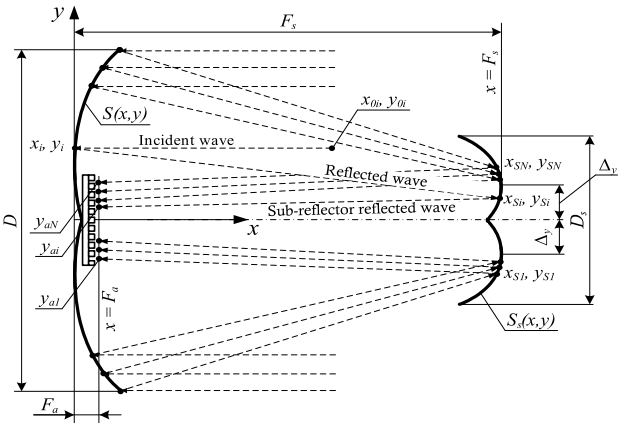

Fig. 12. 2-D center-fed reflector model of a complex double reflector.

TABLE III

OPTIMAL POLYNOMIAL COEFFICIENTS AND DIMENSIONS OF A COMPLEX DOUBLE REFLECTOR FOR WIDE-ANGLE SCANNING UP TO +/−20 (FICTITIOUS MODEL THAT IGNORES BLOCKING)

Variable	Obtained value	Variable	Obtained value
A_{xx}	1.692	B_{xx}	0.116
A_{yy}	1.1285	B_{yy}	-3.768
A_x	-4.922	B_x	-2.862
A_{zz}	1.1285	B_{zz}	-3.768
A_{yz}	0	B_{yz}	0
F_s	0.41 m	F_a	0.1 m
Δ_y	0	$\mathbf{y_0}$	0
$\mathbf{D_s}$	0.89 m	D	0.8 m

this model completely fictitious. The resulting field distribution in the array plane is shown in Fig. 13.

D. Complex Offset Double Reflector

Two optimized versions of the offset double-reflector FPA of Figs. 6 and 7 have been investigated: 1) broadside scan and 2) wide-angle scanning up to ±20° in the azimuth plane.

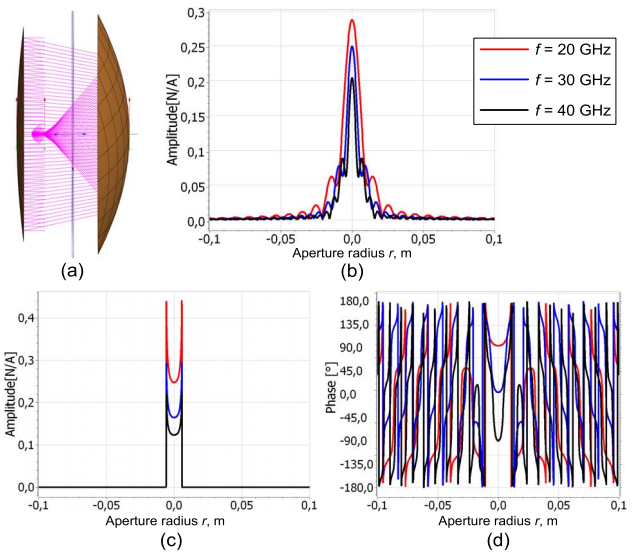

Fig. 13. (a) Complex double-reflector configuration optimized for wide-angle scanning, broadside situation. (b) Electric-field cuts in the array plane based on PO. (c) Electric-field cuts in the array plane based on GO. (d) Phase distribution based on PO simulation in the array plane. Blocking has been ignored.

TABLE IV

OPTIMAL POLYNOMIAL COEFFICIENTS AND DIMENSIONS OF A COMPLEX OFFSET DOUBLE REFLECTOR FOR BROADSIDE SCAN

Variable	Obtained value	Variable	Obtained value
A_{xx}	159	B_{xx}	21
A_{yy}	960	B_{yy}	-886
A_x	-910	B_x	-120
A_{zz}	930	B_{zz}	-935
A_{yz}	0	B_{yz}	0
F_s	0.552 m	F_a	0 m
Δ_y	0 m	Dz_s	0.19 m
z_0	0 m	Dy_s	0.19 m
Ψ	0^0	β	0^0
Z_{off}	0.1 m	D	0.8 m

The wide-angle scanning option has been presented in Section IV-A. For the broadside-scan case, the obtained optimal polynomial coefficients and other relevant dimensions are provided in Table IV.

The discontinuity variable Δ_y is equal to zero, so that both reflectors have a continuous shape. $F_a = 0$ and $\Psi = 0°$, which means that the PAF is located in the center of the coordinate system and is oriented along the yz plane in the model of Figs. 6 and 7. The subreflector dimensions Dz_s and Dy_s are almost a quarter of the main reflector dimension, but due to the offset configuration, no blockage occurs. The field distributions are shown in Fig. 14.

From Fig. 14(c), we can observe that the field distribution is much more uniform as compared to the classical prime-focus reflector. In fact, the performance is similar to the center-fed double-reflector systems but now avoiding blockage of the large subreflector. The phase linearity in the array plane shows an rms error of 1.91° at 30 GHz, which is significantly better than the obtained with the classical prime-focus reflector.

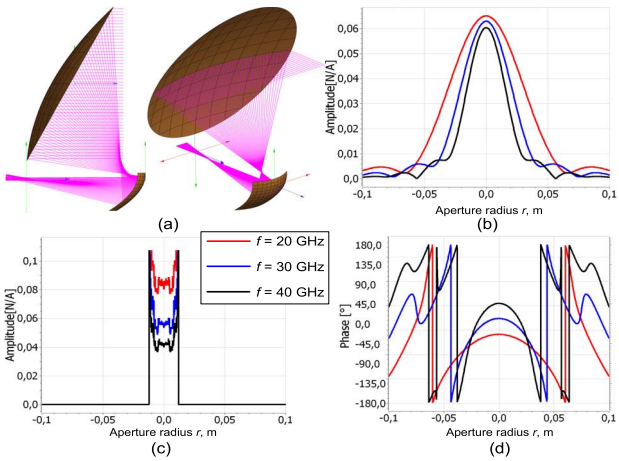

Fig. 14. (a) Offset double-reflector configuration optimized for broadside-scan. (b) Electric-field cuts in the array plane based on PO simulation. (c) Electric-field cuts in the array plane based on GO simulation. (d) Phase distribution based on PO simulation in the array plane.

TABLE V

OPTIMAL POLYNOMIAL COEFFICIENTS AND OTHER DIMENSIONS OF A COMPLEX OFFSET DOUBLE REFLECTOR FOR WIDE-ANGLE SCANNING UP TO +/−20°

Variable	Obtained value	Variable	Obtained value
A_{xx}	0	B_{xx}	30.45
A_{yy}	190	B_{yy}	-168.73
A_x	-550.5	B_x	-124.61
A_{zz}	140.1	B_{zz}	-219.92
A_{yz}	0	B_{yz}	0
F_s	0.79 m	F_a	0 m
z_s	-0.081 m	y_s	-0.102 m
z_0	-0.45 m	z_{s0}	0.49 m
z_{off}	0.1 m	z_c	-0.08 m
Dz_s	0.255 m	Dy_s	0.83 m
Ψ	-27.67^0	β	39.42^0
D	0.8 m		

E. Wide-Scanning Complex Double Reflector

We have optimized the complex offset double reflector for wide-angle scanning. This configuration has been used to construct a prototype for experimental validation, see Section V. For that reason, additional manufacturing-related requirements have been applied for this design. Although the offset configuration allows a large subreflector size, we have limited the dimension to 83 cm. In addition, we have avoided a discontinuity in the surface of the main reflector. Thus, potentially the offset double-reflector configuration could achieve an even better performance if no production limits will be applied. The optimal polynomial coefficients and other relevant dimensions of the optimized complex offset double-reflector of Figs. 6 and 7 for wide-angle scanning are provided in Table V.

In this case, the subreflector of the optimized configuration has a discontinuity since z_s and y_s are not equal to zero. Furthermore, $F_a = 0$ and $\Psi = -27.67°$, which implies that the PAF is located in the center of the coordinate system and has a slight rotation in the offset plane, see also Fig. 6.

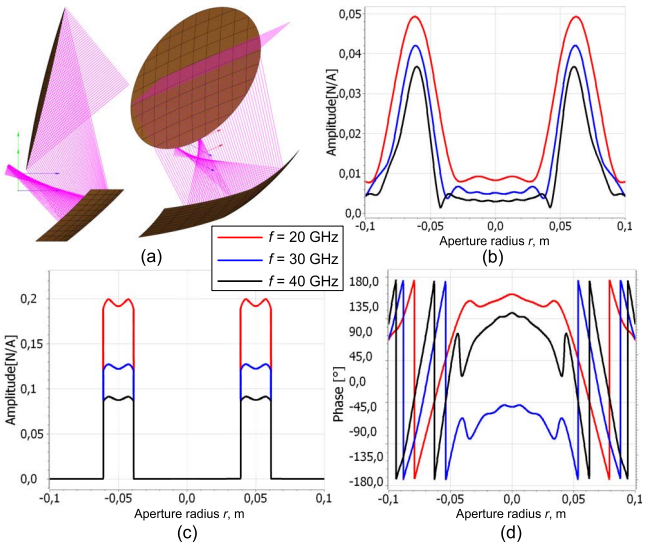

Fig. 15. (a) Optimized complex offset double-reflector configuration for wide-angle scanning, broadside situation. (b) Electric-field cuts in the array plane based on PO simulation. (c) Electric-field cuts in the array plane based on GO simulation. (d) Phase distribution based on PO simulation in the array plane for broadside operation.

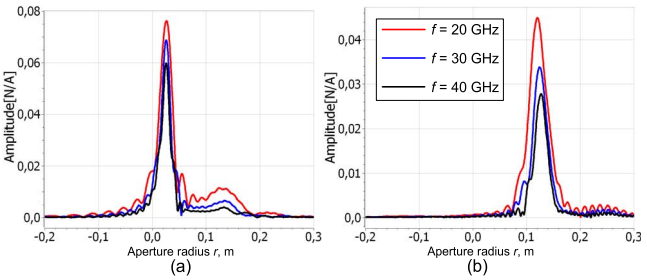

Fig. 16. (a) Electric-field cuts for 10° angle of incidence. (b) Electric-field cuts for 20° angle of incidence based on PO simulation of a complex offset double reflector optimized for wide-angle scanning.

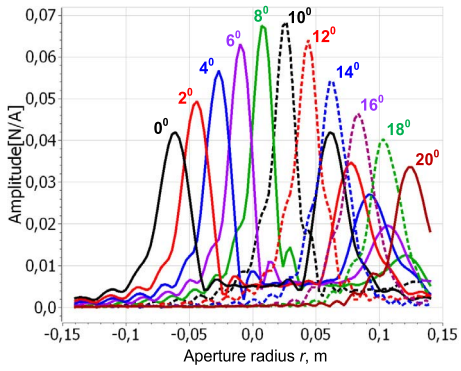

Fig. 17. Electric-field cuts in the array plane of the optimized complex offset double reflector based on PO simulation for various scan angles, $f = 30$ GHz.

The dimensions of the subreflector, Dz_s and Dy_s, are relatively large as compared to the size of the main reflector, but there is no blockage between the reflectors. The field distribution and aperture efficiency for various scan angles of the optimized configuration are shown in Figs. 15–17. Fig. 15 demonstrates the interesting properties of the optimized configuration. In case of broadside operation, the field

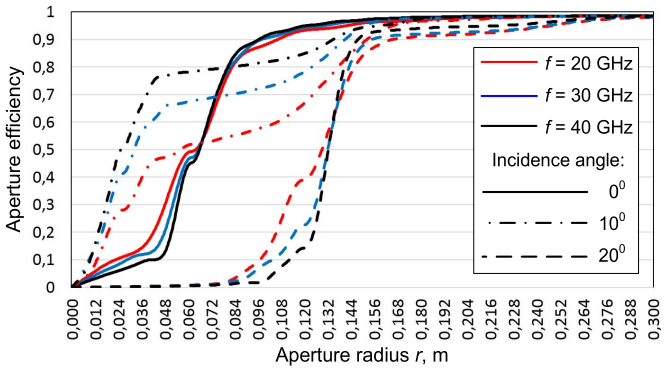

Fig. 18. Aperture efficiency in the array plane for various scan angles of the optimized complex offset double reflector for wide scanning.

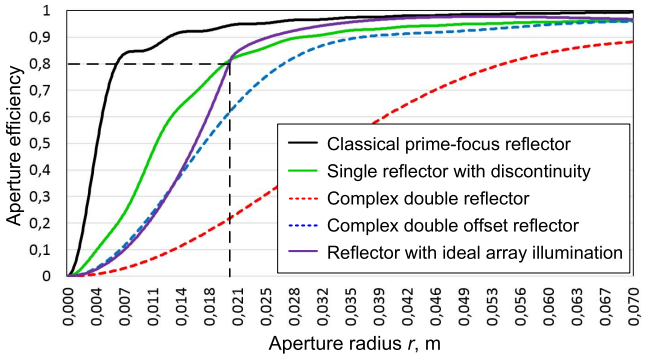

Fig. 19. Realized aperture efficiences of all optimized reflector configurations for broadside operation based on PO simulations, $f = 30$ GHz.

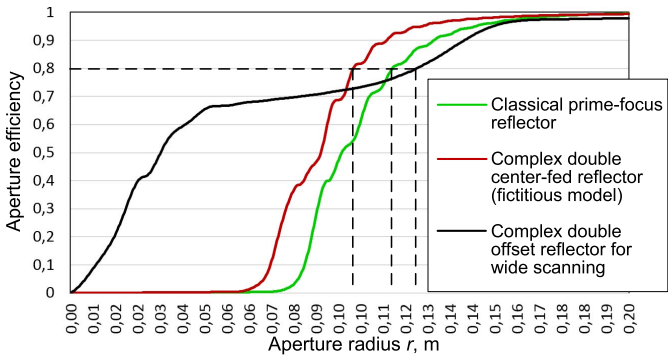

Fig. 20. Comparison of optimized reflector configurations for 10° angle of incidence based on PO simulations, $f = 30$ GHz.

distribution is not focused in the center of the array plane. The subreflector discontinuity creates the bi-focal behavior that results in an extra broadening in case of broadside operation. For scan angles larger than 8°, there is the amplitude dominance of one of the two focal points due to the fact that the illumination is shifted mainly to one of the two subreflector parts.

According to the GO simulation results of Fig. 15(c), the electric-field cuts in the array plane have been split into the two illumination regions with a quite uniform distribution. The PO simulation results of Fig. 15(b) show that the illuminated region for broadside operation is relatively large (about 20 cm) with two distinct field maxima. From PO simulations, we found that for scan angles below 12°,

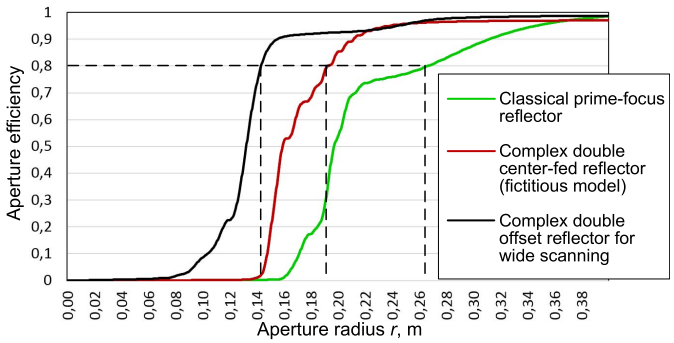

Fig. 21. Comparison of optmized reflector configurations for 20° angle of incidence based on PO simulations, $f = 30$ GHz.

Fig. 22. Photograph of the prototype using a complex offset double reflector setup.

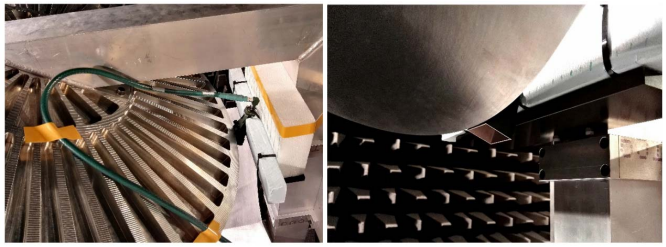

Fig. 23. Photograph of experiments with a horn feed to measure the array-plane field distribution.

the illumination region is smaller as compared to the broadside-scan case. For larger scan angles, between 12° and 20°, the illuminated region is larger than for the broadside-scan case. At the same time, the aperture efficiency distribution (Fig. 18), has a significantly smoother behavior than that of the all other investigated configurations, resulting in a more uniform field distribution over the PAF.

The PAF should have a length of about 28 cm based on an 80% aperture efficiency in order to provide scanning up to ±20° in the azimuth plane. This is significantly better as compared to the scanning capabilities of the classical prime-focus reflector. Moreover, the linearity of the phase distribution at 30 GHz shows an rms error of 2.81°. The PAF width is equal to 4 cm, in line with the results for broadside operation.

F. Comparison of All Configurations

Although a GO-mathematical framework was used to find the optimized geometries, we will use PO to compare the

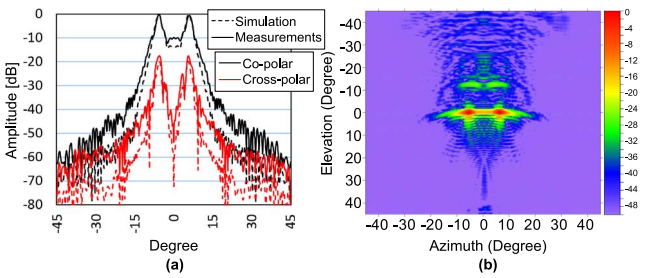

Fig. 24. (a) Far-field pattern in azimuth plane. (b) 2-D far-field image with feed at the center of the array, 30 GHz.

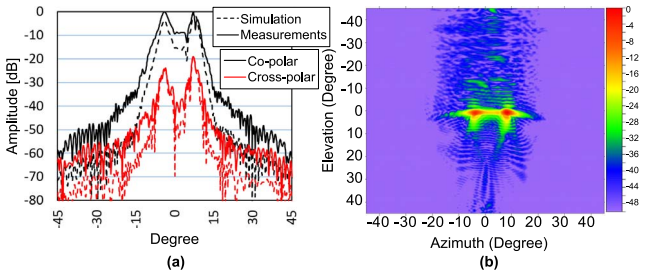

Fig. 25. (a) Far-field pattern in the azimuth plane. (b) 2-D far-field image with feed displacement from the array center 2 cm, 30 GHz.

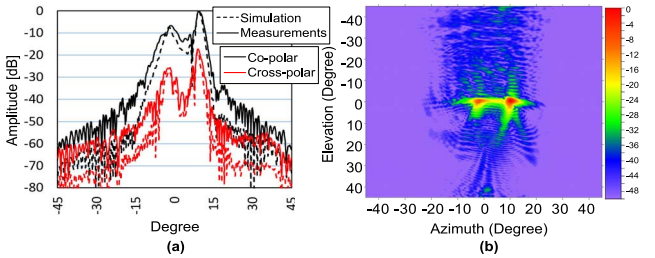

Fig. 26. (a) Far-field pattern in the azimuth plane. (b) 2-D far-field image with feed displacement from the array center 4 cm, 30 GHz.

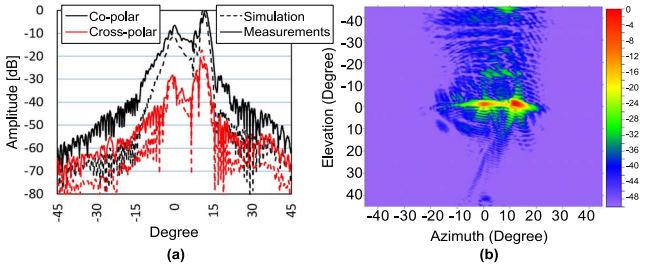

Fig. 27. (a) Far-field pattern in the azimuth plane. (b) 2-D far-field image with feed displacement from the array center 6 cm, 30 GHz.

performance of all configurations. Let us first consider the optimized geometries for broadside operation. Fig. 19 shows the realized aperture efficiencies at the center frequency. The classical prime-focus reflector (Fig. 1) is added as a reference case. In addition, the aperture efficiency for a (nonphysical) reflector that provides an ideal array illumination is also presented in Fig. 19. It is obvious that for any distribution of the electric field in the array plane an aperture efficiency of 100% could only be achieved by using an infinitely large

TABLE VI

COMPARISON OF OPTIMIZED REFLECTOR CONFIGURATIONS FOR BROADSIDE OPERATION, PO SIMULATION MODEL IS USED

Reflector configuration	**Array size (radius) for 80% aperture efficiency at 30 GHz**	**Phase linearity: rms error at 30 GHz**
Reflector with ideal array illumination	**2 cm**	0^0
Classical prime-focus reflector	0.6 cm	6.36^0
Single reflector with discontinuity	**1.95 cm**	$\mathbf{2.02^0}$
Complex double-reflector (including blockage)	5.5 cm	1.45^0
Complex double offset reflector	**2.7 cm**	$\mathbf{1.91^0}$

TABLE VII

COMPARISON OF OPTIMIZED REFLECTOR CONFIGURATIONS FOR WIDE SCANNING OPERATION, BASED ON PO SIMULATIONS

Reflector configuration	**Array size for 80% aperture efficiency at 30 GHz and percent of active elements from the whole array (for $\pm 20^0$ scanning)**			**Phase linearity: rms error at 30 GHz for broadside operation**
	Scanning range			
	$\mathbf{\pm 0^0}$	$\mathbf{\pm 10^0}$	$\mathbf{\pm 20^0}$	
Reflector with ideal array illumination	4 cm 100%	4 cm 100%	4 cm 100%	0^0
Classical prime-focus reflector	1.2 cm 2.3%	23 cm 7.7%	52 cm 19%	6.36^0
Complex double center-fed reflector (fictitious model)	2 cm 5.1%	21 cm 11.5%	39 cm 16.7%	3.28^0
Complex offset double reflector	**16 cm 28%**	**25 cm 44.6%**	**28 cm 21.4%**	$\mathbf{2.81^0}$

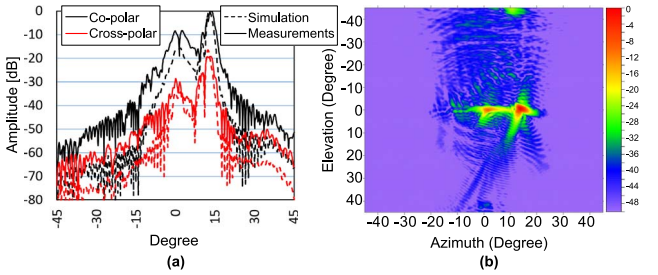

Fig. 28. (a) Far-field pattern in the azimuth plane. (b) 2-D far-field image with feed displacement from the array center 8 cm, 30 GHz.

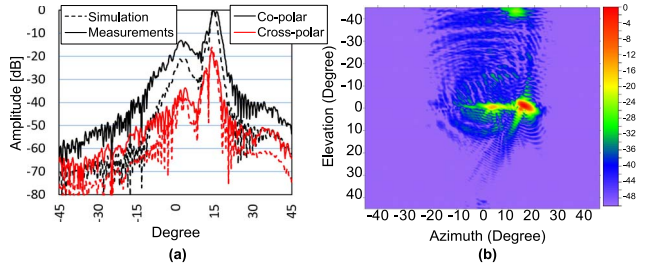

Fig. 29. (a) Far-field pattern in the azimuth plane. (b) 2-D far-field image with feed displacement from the array center 10 cm, 30 GHz.

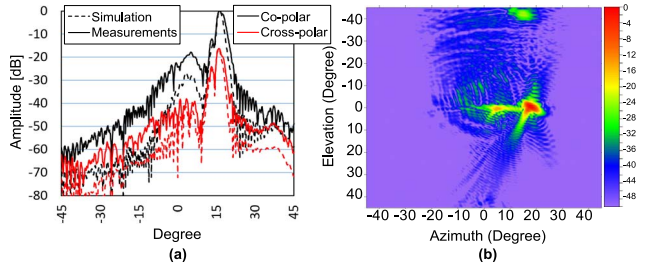

Fig. 30. (a) Far-field pattern in the azimuth plane. (b) 2-D far-field image with feed displacement from the array center 12 cm, 30 GHz.

aperture radius. Therefore, an aperture efficiency of 80% has been chosen as a reference value. Note that the array blockage is included in Fig. 19. Therefore, the aperture efficiency level starts to decrease with increasing size of the aperture radius.

The optimization goal has been set for an array length of 4 or 2 cm array radius. Therefore, the reflector with ideal array illumination reaches an aperture efficiency of 80% at 2 cm radius. The required array size has been estimated for all configurations based on 80% aperture efficiency. Table VI summarizes the required array sizes and the realized phase linearity over the array. According to Fig. 19 and Table VI, the center-fed single reflector with discontinuity provides the best fit with the ideal FPA reflector system. This design includes an axial displacement of the feed array as well. The realized array size is approximately three times larger as compared to the classical prime-focus reflector, which provides a significant increase of the realized EIRP. Nevertheless, according to Fig. 19 the best results for extending the field distribution along the array plane are obtained with the double-reflector configurations (center-fed and offset reflectors). The required array size of the center-fed double reflector is larger than the optimization goal. This can be explained by diffraction effects, which are more significant in the case of center-fed double reflectors [27]. The complex offset double reflector has a higher complexity and achieves the best performance in amplitude and phase uniformity along the array.

A comparison of the performance of the optimized reflector systems in case of wide-angle scanning is provided in Figs. 20 and 21 and Table VII. Note that the complex double center-fed reflector for wide scanning is a fictional (nonphysical) model, since we have ignored the blockage from the large subreflector. We included it, since it shows the potential of the complex double reflector.

By using an offset configuration, a realistic system is obtained. According to Table VII, the best performance is obtained with the complex offset double-reflector configuration. The required array size is almost two times smaller as compared to the classical prime-focus reflector for $\pm 20°$ scanning in the azimuth plane. At the same time, the aperture efficiency has the smoothest distribution along the array, resulting in a high percentage of simultaneously active array elements. For 10° scanning about 44.6% of

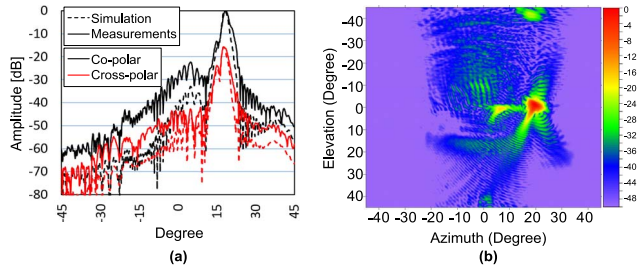

Fig. 31. (a) Far-field pattern in the azimuth plane. (b) 2-D far-field image with feed displacement from the array center 14 cm, 30 GHz.

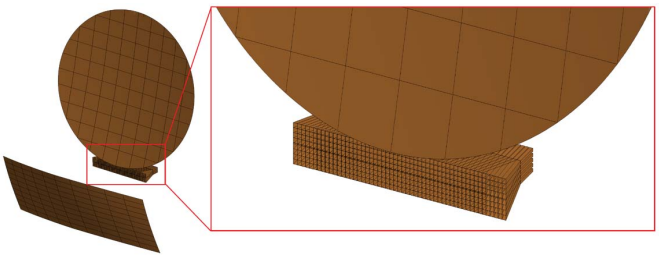

Fig. 32. Complex offset double-reflector configuration fed by an array of horn antennas.

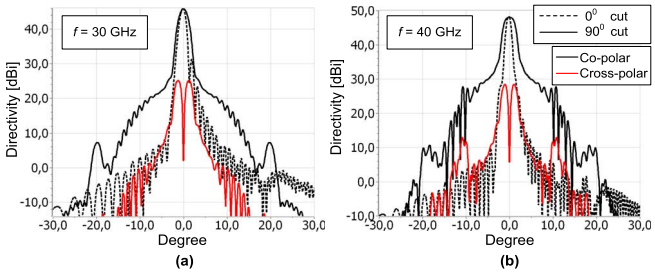

Fig. 33. Directivity of the complex offset double-reflector FPA with element spacing of $0.8\lambda_0$ for (a) $f = 30$ GHz and (b) $f = 40$ GHz.

the array elements are active. Moreover, the complex offset double reflector also provides the best phase linearity. The advantages of this system over the center-fed double-reflector can be explained by the additional design complexity. The optimization of the nonsymmetrical geometry has been done for two orthogonal planes, while for a symmetric center-fed configuration the geometry is the same in all planes. Therefore, independent optimization of scanning and nonscanning planes is a clear advantage of offset configurations.

V. Experimental Validation

A prototype of the optimized complex offset double-reflector was realized and experimentally validated. A photograph of the prototype is shown in Fig. 22 and was measured in the near-field facility at Eindhoven University of Technology.

The array-plane illumination is measured with a horn antenna with a frequency range of 26.4–40.1 GHz, as shown in Fig. 23. Relevant simulation models have been realized in GRASP and simulated by means of PO [15]. To test the required scanning capability up to $\pm 20°$ in the azimuth plane, an experimental validation with a synthesized PAF has been

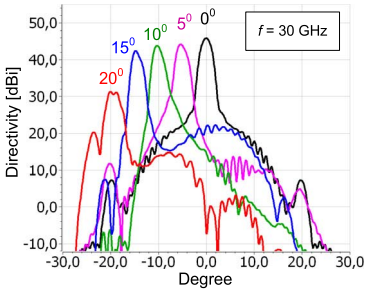

Fig. 34. Directivity of the complex offset double-reflector FPA with element spacing of $0.8\lambda_0$ for different scan angles, $f = 30$ GHz.

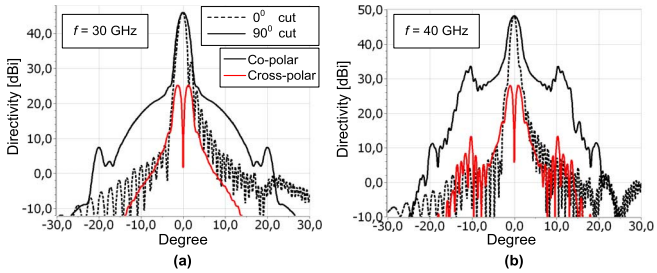

Fig. 35. Directivity of the complex offset double-reflector FPA with element spacing of $0.7\lambda_0$ at 30 GHz for (a) $f = 30$ GHz and (b) $f = 40$ GHz.

done. A horn antenna has been placed in different positions along the array plane and related radiation pattern have been measured. According to Table VII, the array size should be 28 cm. Therefore, we first measured the far-field patterns with the feed located in the center of the array (Fig. 24), and then shifted the feed in steps of 2 cm until it reaches the edge of the array at 14 cm shift (Figs. 25–31). The agreement between simulation and measurement is in all cases quite good. The differences in sidelobe levels are mainly due to the large support structure of the reflector in the prototype of Fig. 22. This was not included in the simulation. Similar to the field distribution in the array plane for the receive case (see Fig. 17), the far-field pattern provides a bi-focal kind of distribution when only a single array element is used. Moreover, the difference between the copolar and cross-polar components of the electric field is sufficiently high and it is not less than 20 dB. For the maximum feed displacement of 14 cm (Fig. 31), the main lobe deviation about 17°. This is less than the required 20°, but could be improved somewhat by using additional phase control.

To prove the scan performance of the realized reflector prototype, we have done additional simulations with an array of horn antennas, as illustrated in Fig. 32. The horn antennas have the same dimensions as used in the experiments. The amplitude and phase of the individual horns have been adjusted by conjugate field matching according to the field distribution in the array plane for the receive case [Fig. 15(b) and (d)]. In this way, it is possible to estimate the reflector directivity using GRASP [15]. Since we have used an ideal horn model, the mutual coupling between array elements is ignored as well as feed mismatch efficiency and phase efficiency. Nevertheless, the radiation efficiency of the reflector, taper efficiency, spill-over efficiency, polarization efficiency is included.

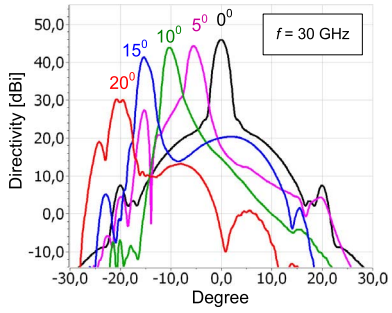

Fig. 36. Directivity of the complex offset double-reflector FPA with element spacing of $0.7\lambda_0$ for different scan angles, $f = 30$ GHz.

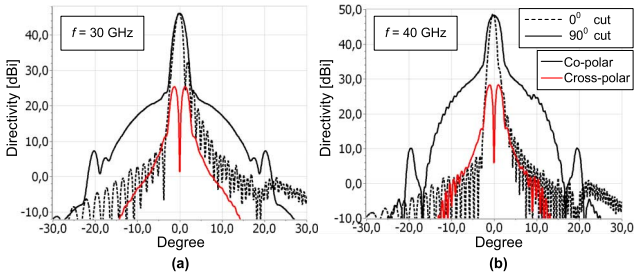

Fig. 37. Directivity of the complex offset double-reflector FPA with element spacing of $0.6\lambda_0$ at 30 GHz for (a) $f = 30$ GHz and (b) $f = 40$ GHz.

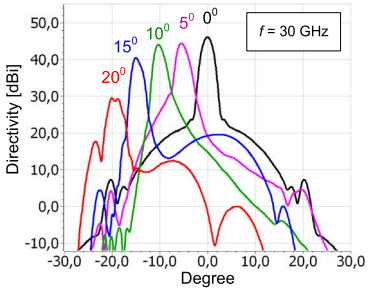

Fig. 38. Directivity of the complex offset double reflector FPA with element spacing of $0.6\lambda_0$ for different scan angles, $f = 30$ GHz.

In other words, all parameters related to the actual reflector design are considered. We have investigated the performance at scan angles 0°, 5°, 10°, 15°, and 20° both for 30 and 40 GHz. In addition, array spacings of $0.6\lambda_0$, $0.7\lambda_0$, and $0.8\lambda_0$ have been applied, where λ_0 is the wavelength at 30 GHz. Figs. 33, 35, and 37 present the performance at broadside of the complex offset double-reflector configuration. The 90° cuts correspond to the scan plane or the azimuth plane. In the 0° plane, the patterns show a similar behavior as classical prime-focus reflectors.

Figs. 34, 36, and 38 show the predicted performance in case of scanning. Excitations of the array elements have been optimized to realize the scanning performance up to 20°. We can observe that for a scanning range of ±15°, the directivity drop is limited to only a few decibels and remains above 40 dBi. This proves the scanning capabilities of this reflector system. The variation in beam directivity across the scan range could be improved by overcoming the prototype production limitations based on the proposed design methods.

TABLE VIII

PERFORMANCE OF THE PROTOTYPE WITH DIFFERENT ARRAY ELEMENT SPACING

Number of array elements (horns) and element spacing (λ_0= 1 cm)	Directivity [dB]		Reflector efficiency	
	Frequency		Frequency	
	30 GHz	40 GHz	30 GHz	40 GHz
180 horns, $0.8\lambda_0$	45.801	48.008	78 %	73 %
200 horns, $0.7\lambda_0$	45.913	48.183	80 %	76 %
230 horns, $0.6\lambda_0$	46.071	48.239	83 %	77 %

Table VIII summarizes the realized directivity and reflector efficiencies. According to Table VIII, there is a tradeoff between the size of the feed array, the number of horn antennas and the realized efficiency. A higher directivity and reflector efficiency is obtained by using a smaller array grid and more array elements. Nevertheless, even a $0.8\lambda_0$ element spacing is physically not possible to realize in practice, since the horn antennas that we used are too large. Therefore, one of the crucial challenges for wideband operation is to investigate array elements which could cover the entire frequency range of 20–40 GHz with a well-behaved embedded element pattern and at the same time have compact dimensions below 0.6 λ_0. Dubok *et al.* [9], [28] describe array concepts that could meet these stringent requirements.

VI. CONCLUSION

In this paper, a mathematical framework, based on GO, is presented to optimize wide-scanning single- and double-reflector FPAs. The suggested evaluation method allows the comparison of all the configurations with an ideal reference case. An optimized new complex offset double-reflector configuration has been designed, produced, and experimentally validated. This FPA system achieves the intended scanning range using a compact array which allows half of the array elements to be active during scanning within the scan range of ±10° and at least a quarter of the array elements active within a scan range of ±20°. The scanning capabilities have been significantly improved as compared to classical prime-focus and double-parabolic reflectors. The well-known FPA problem of a small illuminated region in the focal plane has been successfully solved. In addition, the phase linearity between the array elements of the PAF has been sufficiently improved in order to allow an optical beamforming concept (2.81° rms linearity error at 30 GHz). The experiments demonstrate a very good agreement with simulations and fully prove the required scanning performance within the ±20° scan range with high directivity and reflector efficiency up to 83% at 30 GHz and 77% at 40 GHz.

As a next step, the presented method of GO reflector optimization could be extended to even more complicated reflector shapes. In addition, a study of a wideband PAR using a small element spacing is one of the key elements for future research.

REFERENCES

[1] P. Benthem *et al.*, "Aperture array development for future large radio telescopes," in *Proc. 5th Eur. Conf. Antennas Propag. (EUCAP)*, Apr. 2011, pp. 2601–2605.

[2] A. Zamanifekri and A. B. Smolders, "Optimum configuration of focal plane arrays for satellite communication," in *Proc. IEEE Antennas Propag. Soc. Int. Symp. (APSURSI)*, Jul. 2013, pp. 952–953.
[3] M. Cooley, "Phased array fed reflector (PAFR) antenna architectures for space-based sensors," in *Proc. IEEE Aerosp. Conf.*, Mar. 2015, pp. 1–11.
[4] A. Al-Rawi, A. Dubok, M. H. A. J. Herben, and A. B. Smolders, "Point-to-point radio link variation at E-band and its effect on antenna design," in *Proc. Prog. Electromagn. Res. Symp.*, Prague, Czech Republic, Jul. 2015, pp. 1–6.
[5] D. B. Hayman, T. S. Bird, K. P. Esselle, and P. Hall, "Encircled power study of focal plane field for estimating focal plane array size," in *Proc. IEEE Antennas Propag. Soc. Int. Symp.*, vol. 3A, Jul. 2005, pp. 371–374.
[6] M. Zimmerman, S. W. Lee, B. Houshmand, Y. Rahmat-Samii, and R. Acosta, "A comparison of reflector antenna designs for wide-angle scanning," NASA Technol. Workshop Earth Sci. Geostationary Platforms, Hampton, VA, USA, NASA Tech. Memorandum 101459, Sep. 1988.
[7] M. N. M. Kehn and L. Shafai, "Characterization of dense focal plane array feeds for parabolic reflectors in achieving closely overlapping or widely separated multiple beams," *Radio Sci.*, vol. 44, no. 3, p. 1–25, Jun. 2009.
[8] A. Al-Rawi, A. Dubok, S. J. Geluk, B. P. de Hon, M. H. A. J. Herben, and A. B. Smolders, "Increasing the EIRP by using FPA-fed reflector antennas," in *Proc. IEEE Int. Symp. Antennas Propag. (APSURSI)*, Fajardo, Puerto Rico, Jun./Jul. 2016, pp. 1623–1624.
[9] A. Dubok, A. Al-Rawi, M. H. A. J. Herben, and A. B. Smolders, "Wideband focal plane connected array," in *Proc. 10th Eur. Conf. Antennas Propag. (EuCAP)*, Davos, Switzerland, Apr. 2016, pp. 1–5.
[10] A. M. Ferendeci, "Smart electronic phase control for phased array antennas," in *Proc. IEEE Nat. Aerosp. Electron. Conf.*, Fairborn, OH, USA, Jul. 2010, pp. 250–252.
[11] *FREEBEAM Project*. [Online]. Available: https://www.nwo.nl/onderzoek-en-resultaten/onderzoeksprojecten/i/58/9058.html
[12] D. Marpaung, C. Roeloffzen, R. Heideman, A. Leinse, S. Sales, and J. Capmany, "Integrated microwave photonics," *Laser Photon. Rev.*, vol. 7, no. 4, pp. 506–538, Jul. 2013.
[13] M. Burla *et al.*, "Multiwavelength-integrated optical beamformer based on wavelength division multiplexing for 2-D phased array antennas," *J. Lightw. Technol.*, vol. 32, no. 1, pp. 3509–3520, Oct. 15, 2014.
[14] N. Tessema, Z. Cao, A. Dubok, E. Tangdiongga, A. B. Smolders, and A. M. J. Koonen, "A Si3N4 PIC for optically controlled 2D radio beamforming in satellite communications," in *Proc. Int. Top. Meeting Microw. Photon. (MWP)*, Paphos, Cyprus, Oct. 2015, pp. 1–4.
[15] *TICRA Software*. [Online]. Available: http://www.ticra.com/products/software/grasp
[16] H. C. Minnett and B. M. Thomas, "Fields in the image space of symmetrical focusing reflectors," *Proc. Inst. Elect. Eng.*, vol. 115, no. 10, pp. 1419–1430, Oct. 1968.
[17] A. Dubok *et al.*, "Double-reflector configuration for optimal exposure of wideband focal-plane arrays with optical beamforming," *IEEE Trans. Antennas Propag.*, vol. 65, no. 8, pp. 4316–4321, Aug. 2017, doi: 10.1109/TAP.2017.2709620.
[18] A. H. Guenther, L. S. Pedrotti, and C. Roychoudhuri, *Fundamentals of Photonics*. Storrs, CT, USA: Univ. of Connecticut Press, 2000.
[19] F. J. da Silva Moreira and J. R. Bergmann, "Classical axis-displaced dual-reflector antennas for omnidirectional coverage," *IEEE Trans. Antennas Propag.*, vol. 53, no. 9, pp. 2799–2808, Sep. 2005.
[20] B. S. Westcott, F. A. Stevens, and F. Brickell, "GO synthesis of offset dual reflectors," *IEE Proc. H-Microw., Opt. Antennas*, vol. 128, no. 1, pp. 11–18, Feb. 1981.
[21] M. Born *et al.*, *Principles of Optics: Electromagnetic Theory of Propagation, Interference and Diffraction of Light*. Cambridge, U.K.: Cambridge Univ. Press, 1999.
[22] S. Morgan, "Some examples of generalized cassegrainian and gregorian antennas," *IEEE Trans. Antennas Propag.*, vol. 12, no. 6, pp. 685–691, Nov. 1964.
[23] C. Dragone and M. J. Gans, "Imaging reflector arrangements to form a scanning beam using a small array," *Bell Syst. Tech. J.*, vol. 58, no. 2, pp. 501–515, Feb. 1979.
[24] A. Dubok, A. Al-Rawi, M. H. A. J. Herben, G. Gerini, and A. B. Smolders, "Wide-angle scanning reflector configuration for focal plane arrays," in *Proc. IEEE Int. Symp. Antennas Propag. (APSURSI)*, Fajardo, Puerto Rico, Jun./Jul. 2016, pp. 1625–1626.
[25] F. Pelorossi, G. Toso, and P. Angeletti, "On the scanning properties of imaging antennas based on dual confocal paraboloidal reflectors," *Prog. Electromagn. Res.*, vol. 37, pp. 95–107, Sep. 2014.
[26] G. Toso, "The beauty of multibeam antennas," in *Proc. 9th Eur. Conf. Antennas Propag. (EuCAP)*, Lisbon, Portugal, Apr. 2015, pp. 1–5.
[27] S. G. Hay, "A double-edge-diffraction Gaussian-series method for efficient physical optics analysis of dual-shaped-reflector antennas," *IEEE Trans. Antennas Propag.*, vol. 53, no. 8, pp. 2597–2610, Aug. 2005.
[28] A. Dubok, A. Al-Rawi, M. H. A. J. Herben, and A. B. Smolders, "Fundamental challenges for wideband antenna elements in focal-plane arrays," in *Proc. 9th Eur. Conf. Antennas Propag. (EuCAP)*, Lisbon, Portugal, Apr. 2015, pp. 1–6.

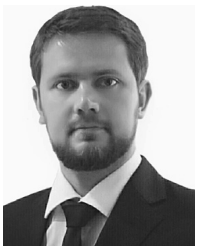

Aleksei Dubok (S'10) was born in Pskov, Russia, in 1987. He received the bachelor's and master's degrees *(cum laude)* from Saint Petersburg State Electrotechnical University, Saint Petersburg, Russia, in 2008 and 2010, respectively, with a focus on microwave and optical and digital means of telecommunications, the second master's degree from the Lappeenranta University of Technology, Lappeenranta, Finland, in 2011, with a focus on electrical engineering and power electronics, the Professional Doctorate in Engineering from the Eindhoven University of Technology, Eindhoven, The Netherlands, in 2013, with a focus on information and communication technology. From 2013 to 2017, he was a Ph.D. candidate in the same group with a focus on planar reflector phased array antenna for multiple applications.

From 2007 to 2010, he was an Engineer-Developer of communications systems at TELROS integration, Saint Petersburg. In 2013, he finalized the post-master's program at the Eindhoven University of Technology. He was involved in the design of an antenna-in-package solution for RFID tags. Since 2017, he has been a Guest Researcher in the same group. Also since 2017, he is an RF Designer at Philips focused on the field of RF hardware development and patient safety for MRI. His current research interests include phased arrays antennas, reflector antennas, frequency selective surfaces, SAR and RF safety, near-field interaction, electromagnetic compatibility, wireless communications, telecommunication systems, and imaging and RF applications in medicine.

Mr. Dubok is an ESMRMB Member.

Ali Al-Rawi (S'13) was born in Baghdad, Iraq, in 1985. He received the master's degree in radio and space science from the Chalmers University of Technology, Gothenburg, Sweden, in 2013. He is currently pursuing the Ph.D. degree with the Department of Electrical Engineering, Electromagnetics Group, Eindhoven University of Technology, Eindhoven, The Netherlands.

His research interests include high-frequency methods, reflector antennas design, and antenna arrays.

Giampiero Gerini (M'92–SM'08) received the M.Sc. degree *(summa cum laude)* and the Ph.D. degree in electronic engineering from the University of Ancona, Ancona, Italy, in 1988 and 1992, respectively.

From 1992 to 1994, he was an Assistant Professor of electromagnetic fields at the University of Ancona. From 1994 to 1997, he was a Research Fellow at the European Space Research and Technology Centre, Noordwijk, The Netherlands, where he was with the Radio Frequency System Division. Since 1997, he has been with the Netherlands Organization for Applied Scientific Research (TNO), Hague, The Netherlands, where he was a Chief Senior Scientist of the Antenna Unit in the Radar Technology Department, TNO Defence Security and Safety, from 1997 to 2013. In 2014, he joined the Optics Department, where he was in-charge of the Metamaterial Research Program. In 2007, he joined the Faculty of Electrical Engineering, Eindhoven University of Technology, Eindhoven, The Netherlands, as a part-time Professor, and where he was a Chair on "Novel Structures and Concepts for Advanced Antennas". Since 2017, he has been the new Chair on "Material Engineering from Microwaves to Optics". His current research interests include phased arrays antennas, electromagnetic bandgap structures, frequency selective surfaces, metamaterials and metasurfaces (from microwave up to optical frequencies), and imaging, metrology, radar and telecommunication systems.

Dr. Gerini was a co-recipient of the 2008 H. A. Wheeler Applications Prize Paper Award of the IEEE Antennas and Propagation Society, the Best Innovative Paper Prize of the 30th ESA Antenna Workshop in 2008, and the Best Antenna Theory Paper Prize of the European Conference on Antennas and Propagation in 2010.

A. Bart Smolders (SM'97) was born in Hilvarenbeek, The Netherlands, in 1965. He received the M.Sc. and Ph.D. degrees in electrical engineering from the Eindhoven University of Technology (TU/e), Eindhoven, The Netherlands, in 1989 and 1994, respectively.

From 1989 to 1991, he was an IC Designer at FEL-TNO, Hague, The Netherlands. From 1994 to 1997, he was a Radar System Designer with Thales, Hengelo, The Netherlands. From 1997 to 2000, he was a Project Leader of the square kilometer array with the Netherlands Foundation for Research in Astronomy, Dwingeloo, The Netherlands. From 2000 to 2010, he has been with NXP (formerly Philips) Semiconductors, The Netherlands, where he was responsible for the innovation in the RF business line. Since 2010, he has been a Full-Time Professor with the Electromagnetics Group, TU/e, with a special interest in antenna systems and applications, where he is currently the Dean of the Electrical Engineering Department. He currently leads several research projects in the area of integrated antenna systems operating at frequencies up to 120 GHz for several application domains, including 5G/6G wireless communications, radar sensors and radio-astronomy. He has authored over 140 papers.

Dr. Smolders is a Junior Past Chairman of the IEEE Benelux section and Past Chair of the NERG (Nederlands Radio- en Elektronica Genootschap). He is a Board Member of the Stichting Wetenschappelijke Activiteiten van het Nederlands URSI Committee and a member of the Advisory Board of ASTRON.